COMMUNICATION

Check for updates

Efficient co-production of ammonia and formic acid from nitrate and polyester *via* paired electrolysis†

Mengmeng Du,‡[a] Tao Sun, ‡[b] Xuyun Guo,‡[c] Mingzhu Han,‡[a] Yu Zhang, ⋆[ad]
Wenxuan Chen,[a] Mengxiang Han,[a] Jizhe Ma,[a] Wenfang Yuan,[a] Chunyu Zhou,[b]
Valeria Nicolosi,[c] Jian Shang,⋆[e] Ning Zhang ⋆[fg] and Bocheng Qiu ⋆[a]

Paired electrolysis, which integrates a productive cathodic reaction, such as the nitrate reduction reaction (NO_3^-RR) with selective oxidation at the anode, offers an intriguing way to maximize both atomic and energy efficiency. However, in a conventional design, the NO_3^-RR is often coupled with the anodic oxygen evolution reaction, leading to substantial energy consumption while yielding low-value oxygen. Here, we report a hybrid electrolysis system that combines cathodic reduction of nitrate to ammonia and anodic oxidation of polyethylene-terephthalate-derived ethylene glycol (EG) to formic acid (FA), utilizing oxygen-vacancy-rich (O_V) Co_3O_4 and Cu doped $Ni(OH)_2$ as the cathode and anode, respectively. Remarkably, this paired electrolysis system demonstrates a faradaic efficiency (FE) of 92% for cathodic ammonia production and a FE of 99% for anodic FA production, while reducing the cell voltage by 0.54 V compared to the conventional NO_3^-RR system at the same current density of 100 mA cm^{-2}. Experimental investigations combined with theoretical calculations reveal that the O_V introduction effectively addresses the insufficient NO_3^- adsorption and hydrogenation on bare Co_3O_4. Additionally, Cu incorporation increases the Ni−O covalency, resulting in an improved EG adsorption ability. This work presents a promising way for waste management *via* paired electrolysis.

New concepts

Electrochemical ammonia (NH_3) production from nitrate-containing wastewater streams presents a sustainable route to concurrent chemical synthesis and waste management, which is thus recognized as an alternative to the conventional, energy-intensive Haber–Bosch process. However, the nitrate (NO_3^-) reduction reaction (NO_3^-RR) typically pairs with the oxygen evolution reaction (OER) at the anode that suffers from sluggish kinetics and high energy input while yielding low-value oxygen. To tackle this issue, we implement paired electrolysis that couples the cathodic NO_3^-RR with anodic oxidation of plastic-derived ethylene glycol. This integrated system enables simultaneous valorization of nitrate wastewater and upcycling of plastic waste within a single electrolyzer, thereby maximizing the utilization of waste resource. This study offers an environmentally benign and energy-efficient pathway for transforming waste streams into valuable chemicals.

Introduction

Ammonia (NH_3) plays a crucial role in the production of fertilizers and is recognized as a critical precursor for the synthesis of a plethora of nitrogen-containing chemicals, including urea and amino acids.[1–3] The industrial-scale NH_3 synthesis is currently being implemented *via* the Haber–Bosch process, which, however, features energy-intensive nature and high carbon emission.[4–6] The electrochemical nitrate (NO_3^-) reduction reaction (NO_3^-RR) driven by renewable electricity

[a] *Jiangsu Key Laboratory of Pesticide Sciences, Department of Chemistry, College of Sciences, Nanjing Agricultural University, Nanjing, 210095, China*

[b] *Department of Radiology, Xinqiao Hospital, Army Medical University, Chongqing, 400037, China*

[c] *School of Chemistry, Centre for Research on Adaptive Nanostructures and Nanodevices (CRANN) and Advanced Materials Bio-Engineering Research Centre (AMBER), Trinity College Dublin, Dublin, D02PN40, Ireland*

[d] *College of Energy and Power Engineering, Nanjing Institute of Technology, Nanjing, 211167, China. E-mail: yu_zhang1225@163.com*

[e] *Low-Dimensional Energy Materials Research Center, Shenzhen Institute of Advanced Technology, Chinese Academy of Sciences, Shenzhen, 518055, China. E-mail: jian.shang@siat.ac.cn*

[f] *Key Laboratory of Precision and Intelligent Chemistry, Department of Environmental Science and Engineering, University of Science and Technology of China, Hefei, 230026, China. E-mail: zhangning18@ustc.edu.cn*

[g] *Sustainable Energy and Environmental Materials Innovation Center, Suzhou Institute for Advanced Research, University of Science and Technology of China, Suzhou, 215123, China*

† Electronic supplementary information (ESI) available. See DOI: https://doi.org/10.1039/d5mh00130g

‡ These authors contributed equally to this work.

offers a cost-effective and low-carbon way for sustainable NH_3 production.[7–10] The NO_3^-RR for NH_3 production involves a sluggish eight-electron transfer kinetics, which necessitates catalysts endowed with abundant active sites.[11–14] Moreover, the byproducts (*e.g.*, NO_2^-, N_2, and NH_2OH) evolved in the NO_3^-RR and the competitive hydrogen evolution reaction (HER) significantly impede the selectivity and current efficiency of the NO_3^-RR.[15–17] Thus far, developing high-performance electrocatalysts for the NO_3^-RR remained a huge challenge, primarily due to the limited understanding of the catalytic mechanism and the structure–activity relationship.

Spinel oxides, characterized by their tetrahedral and octahedral coordination centers, such as Co_3O_4, have garnered substantial interest in the NO_3^-RR, potentially owing to their tunable electronic structure and rich redox chemistry.[18–20] Furthermore, the octahedral Co^{3+} sites with empty d orbitals exhibit a higher affinity for atomic hydrogen adsorption (*H), which thereby serve as hydrogenation centers in converting NO_2^- to NH_3.[21,22] In spite of these aforementioned advantages, bare Co_3O_4 encounters several limitations in the NO_3^-RR, particularly poor NO_3^- adsorption capability, which arises from the elevated energy of the lowest unoccupied molecular π^* orbital (LUMO π^*) of NO_3^-.[23,24] Defect engineering has been deemed as a powerful tool for optimizing the reaction intermediate adsorption on spinel structures.[25–27] Notably, the incorporation of an oxygen vacancy (O_V) into Co_3O_4 leads to an upshift of the d-band center of Co 3d orbitals. This contributes to charge injection into the π^* orbitals of NO_3^-, thus facilitating promoting NO_3^- adsorption and activation.

In this context, creation of an O_V in Co_3O_4 can be expected to play a pivotal role in transforming NO_3^- into NO_2^-.

However, further enhancement of the overall performance of the NO_3^-RR still remains essential for its widespread application. Notably, a limiting factor increasing the energy input of the conventional system is the anodic oxygen evolution reaction (OER), which requires a high oxidative potential yet produces low-cost oxygen (O_2).[28–30] Electrochemical oxidation of plastic-derived feedstocks, benefitting from the low operation potential and the production of value-added chemicals, represents a promising alternative to the OER.[31–34] Consequently, integrating the NO_3^-RR and plastic upcycling into one electrolyzer is anticipated to yield valuable chemicals at minimal investment. Nevertheless, the operational stability and economic feasibility of this paired system still face challenges.

Herein, we designed a paired electrochemical system that couples the cathodic NO_3^-RR for NH_3 production with anodic polyethylene-terephthalate-derived (PET-derived) ethylene glycol (EG) oxidation for formic acid (FA) evolution. Through constructing an oxygen vacancy Co_3O_4 (O_V–Co_3O_4) cathode and a Cu doped $Ni(OH)_2$ (Cu–$Ni(OH)_2$) anode, we achieved a FE of NH_3 (92%) at the cathode and a FE of FA (99%) at the anode at 100 mA cm^{-2}. Based on experimental observations and theoretical insights into the improved ability for NO_3^- adsorption and activation on O_V–Co_3O_4, as well as the enhanced EG binding on Cu–$Ni(OH)_2$, we propose a continuous co-production of NH_4Cl and formate from liter-scale

nitrate wastewater and hundred-gram-scale PET bottles. Techno-economic analysis (TEA) suggests that this paired electrolysis system remains profitable, thus attracting industrial investment.

Results and discussion

Cathode catalyst characterization studies

The preparation procedure of the O_V–Co_3O_4 cathode initiates with the growth of Co(OH)F nanorods on Ni foam (Co(OH)F/NF) through a hydrothermal method (Fig. 1a). Scanning electron microscopy (SEM) and X-ray diffraction (XRD) patterns clearly show the uniform growth of Co(OH)F nanorods throughout the entire NF substrate (Fig. S1 and S2, ESI†). The following calcination treatment in air successfully achieves the conversion of Co(OH)F/NF into Co_3O_4/NF, as evidenced by the SEM and transmission electron microscopy (TEM) observations (Fig. S3 and S4, ESI†). The O_V is subsequently introduced into Co_3O_4 *via* reduction treatment in a H_2 atmosphere for 1 h. Unless otherwise specified, the O_V–Co_3O_4/NF catalyst refers to the sample subjected to H_2 reduction for 1 h. The crystal structure of O_V–Co_3O_4 is elucidated by using XRD analysis, which reveals all the peaks observed corresponding to the standard spinel structure (Fig. 1b). Furthermore, SEM and TEM observations collectively exhibit the retention of the nanorod morphology in O_V–Co_3O_4 (Fig. 1c and d). Selected area electron diffraction (SAED) patterns (Fig. 1d, inset) exhibit the exposure of the characteristic (220), (311), (400), and (511) planes of Co_3O_4. High-resolution TEM reveals a set of lattice fringes with a spacing of 0.24 nm (Fig. 1e), which is assigned to the (311) plane of Co_3O_4.[35] High-angle annular dark field scanning TEM (HAADF-STEM) imaging and electron energy loss spectroscopy (EELS) demonstrate the uniform distribution of Co and O elements throughout the O_V–Co_3O_4 nanorod (Fig. 1f). The O_V was identified by electron spin resonance (ESR) spectra (Fig. 1g), in which a weak ESR signal at g = 2.002 is observed for Co_3O_4. In contrast, O_V–Co_3O_4 exhibits a significantly enhanced O_V signal, suggesting the successful introduction of O_V. The O_V introduction inevitably leads to a change in the valence state of Co atoms adjacent with O_V. As illustrated in Co 2p X-ray photoelectron spectroscopy (XPS) (Fig. 1h), the proportion of Co^{2+} is substantially improved from 39% to 87% after O_V introduction, which is attributed to the transformation of octahedral Co^{3+} to Co^{2+} upon O_V incorporation.[36] Furthermore, the local electrons at the O_V sites have the potential to reduce the adsorbed water molecule to hydrogen and hydroxyl.[37,38] This phenomenon accounts for the higher content of surface hydroxyls on O_V–Co_3O_4/NF (79%) compared with bare Co_3O_4/NF (22%), as observed in the O 1s XPS spectra (Fig. 1i).

NO_3^-RR activity and mechanism analysis

The electrochemical NO_3^-RR activity of O_V–Co_3O_4/NF was measured in a three-electrode H-type cell under ambient conditions. Colorimetric methods, utilizing a calibration curve
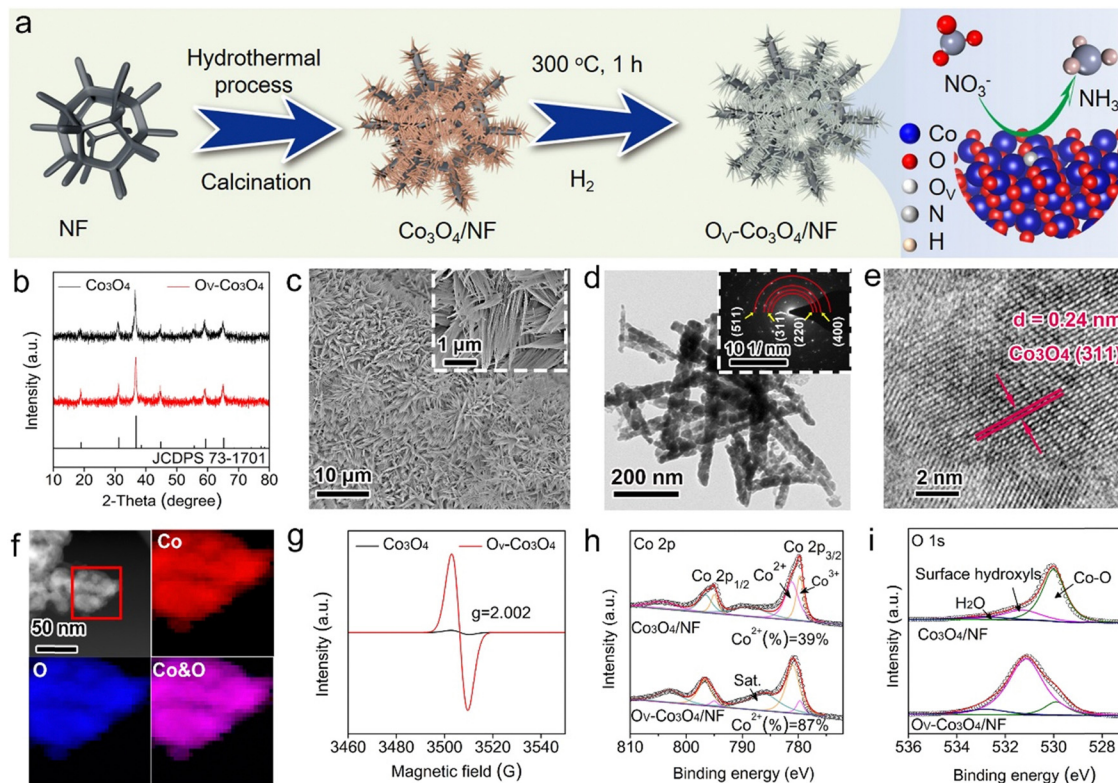
Fig. 1 Morphology and structure characterization of the cathode catalyst. (a) Schematic illustration of the O_V–Co_3O_4/NF preparation process. (b) XRD patterns of Co_3O_4 and O_V–Co_3O_4 powders scraped from the Ni substrate. (c) SEM image, (d) TEM image (the inset shows the corresponding SAED patterns), (e) HRTEM image, (f) HAADF-STEM image and its corresponding EELS maps of O_V–Co_3O_4. (g) ESR spectra of O_V–Co_3O_4 and Co_3O_4 powders scraped from the NF substrate. (h) Co 2p and (i) O 1s XPS spectra of Co_3O_4/NF and O_V–Co_3O_4/NF.

(Fig. S5, ESI†), were employed to quantitatively determine ammonia concentrations. All potentials are referenced to the reversible hydrogen electrode (RHE), unless otherwise specified. A slight enhancement in the HER activity can be observed for O_V–Co_3O_4/NF relative to Co_3O_4/NF in the absence of NO_3^- (Fig. 2a). Upon NO_3^- addition, O_V–Co_3O_4/NF enables a dramatically increased current density compared with Co_3O_4/NF, highlighting the key role of O_V in the NO_3^-RR. To evaluate the NO_3^-RR performance more fairly, specific activities were calculated by normalizing linear sweep voltammetry (LSV) curves with the electrochemical active surface area (ECSA) (Fig. S6, ESI†). The results suggest that the O_V–Co_3O_4/NF still allows better NO_3^-RR activity than Co_3O_4/NF. Additionally, O_V–Co_3O_4/NF exhibits more favorable reaction kinetics and enhanced charge transfer than Co_3O_4/NF, as corroborated by the reduced Tafel slope and charge transfer resistance (Fig. S7 and S8, ESI†).

The FE and productivity of NH_3 over O_V–Co_3O_4/NF and Co_3O_4/NF were measured to reveal the role of O_V. As presented in Fig. 2b, O_V–Co_3O_4/NF exhibits a higher FE of NH_3 compared with Co_3O_4/NF across a wide potential range from -0.1 to -0.45 V. Impressively, O_V–Co_3O_4/NF achieves a maximum FE of 95.2% at -0.3 V, which outperforms most of recently reported NO_3^-RR catalysts (Table S1, ESI†). Additionally, O_V–Co_3O_4/NF displays an NH_3 productivity of 0.31 mmol cm^{-2} h^{-1}

at -0.3 V, notably higher than that of bare Co_3O_4/NF (0.17 mmol cm^{-2} h^{-1}). This enhanced performance is attributed to the promotion of NO_3^- adsorption and activation by O_V, thus accelerating the NO_3^--to-NO_2^- conversion step and improving the NH_3 yield rate.

To identify the impact of the O_V concentration on the NO_3^-RR, O_V–Co_3O_4/NF with varying O_V contents were synthesized by adjusting the reductive treatment time in a H_2 atmosphere (Fig. S9 and S10, ESI†). The results indicate that the O_V–Co_3O_4/NF catalyst treated with H_2 reduction for 1 h exhibits the highest FE and productivity of NH_3. To exclude the environmental contaminants in NH_3 detection, isotope-labeling tests were carried out (Fig. 2c). The results confirm that the produced NH_3 originates from the NO_3^-RR rather than the environmental contaminants. The electrochemical NO_3^-RR durability of O_V–Co_3O_4/NF was assessed in ten consecutive cycles (Fig. 2d). The productivity and FE of NH_3 exhibited slight fluctuations in each cycle but remained stable. Strikingly, no obvious changes in morphology, crystal structure, and chemical state can be observed for the recovered O_V–Co_3O_4/NF, as confirmed by a combination of SEM, TEM, XRD, and XPS characterization studies (Fig. S11–S13, ESI†).

The role of O_V in the NO_3^-RR was further investigated *via* density functional theory (DFT) calculations (Fig. S14, ESI†). Note that the distance between the Co 3d and O 2p band
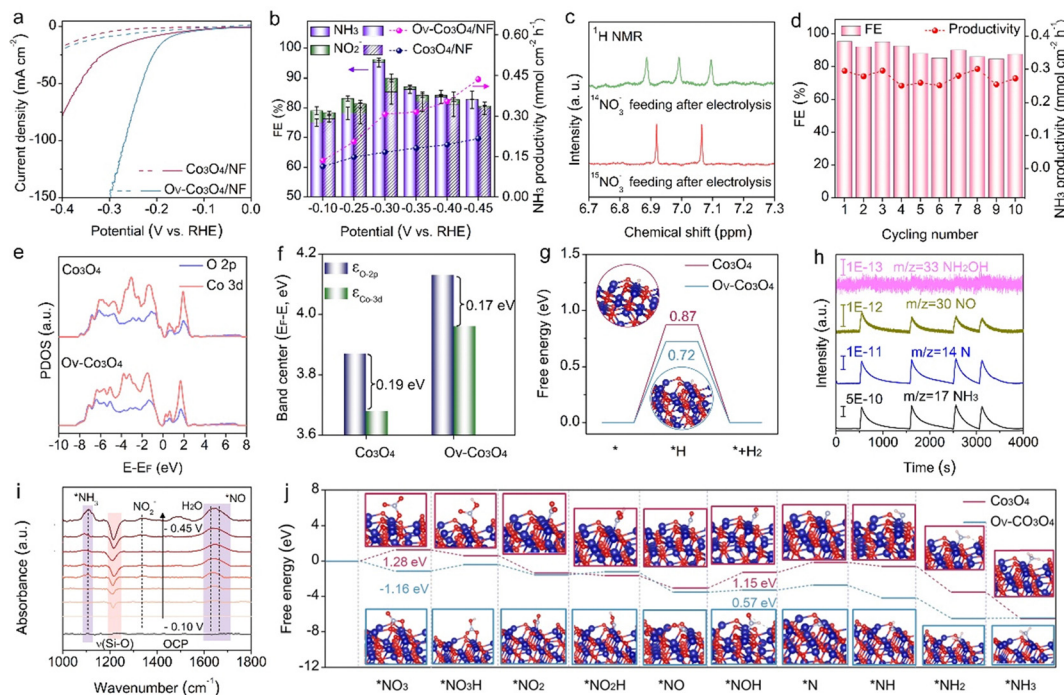
Fig. 2 NO_3^-RR activity and enhanced mechanism. (a) Polarization curves of Co_3O_4/NF and O_V–Co_3O_4/NF in 1 M KOH solution with (solid line) and without (dotted line) 0.1 M NO_3^-. (b) The NO_3^-RR activity comparison between Co_3O_4/NF and O_V–Co_3O_4/NF. (c) ^{1}H NMR spectra of post-reaction electrolytes using $^{15}NO_3^-$ and $^{14}NO_3^-$ feedstocks. (d) Cycling experiments of O_V–Co_3O_4/NF for the NO_3^-RR conducted at −0.3 V. (e) PDOS of the (311) planes of Co_3O_4 and O_V–Co_3O_4. (f) The band center calculations of O 2p and Co 3d in Co_3O_4 (311) and O_V–Co_3O_4 (311). (g) The Gibbs free energy for H adsorption over Co_3O_4 (311) and O_V–Co_3O_4 (311). (h) In situ DEMS analysis of nitrogen-containing intermediates during the NO_3^-RR over O_V–Co_3O_4/NF. (i) In situ FTIR spectra of the NO_3^-RR over O_V–Co_3O_4/NF recorded under varying potentials. (j) Free energy diagram of each intermediate state within the NO_3^-RR on Co_3O_4 (311) and O_V–Co_3O_4 (311).

centers (denoted as D_M) is recognized as a descriptor of the degree of Co–O covalency, with a smaller D_M indicating an increased Co–O covalency.[39,40] The partial density of state (PDOS) combined with the band center calcination reveals that O_V–Co_3O_4 enables a reduced D_M value (0.17 eV) compared with bare Co_3O_4 (0.19 eV), suggesting a higher overlap between Co 2p and O 1s in O_V–Co_3O_4 (Fig. 2e and f). Such improved Co–O covalency contributes to the NO_3^- adsorption and activation.[41] Moreover, the O_V sites promote the generation of active adsorbed H (H*), as indicated by the free energy for H* evolution being closer to zero on O_V–Co_3O_4 compared to Co_3O_4 (Fig. 2g). The enhanced activity for H* generation on O_V–Co_3O_4 contributes to the hydrogenation of NO_2^- to NH_3.[42]

The reaction pathway was identified using in situ differential electrochemical mass spectrometry (DEMS). There exist two potential pathways for the conversion of NO_3^- to NH_3, as illustrated in Fig. S15 (ESI†). The appearance of *NO signal, coupled with the absence of *NH_2OH signal, implies that NH_3 is most likely formed via the *NOH intermediate pathway (Fig. 2h). In situ Fourier transform infrared (FTIR) spectroscopy was employed to differentiate the reaction intermediates (Fig. 2i). The peaks at 1338 and 1665 cm^{-1} are ascribed to *NO_2^- and *NO intermediate species, respectively.[43] Note that the absence of the characteristic NH_2OH band in FTIR is consistent with the results of in situ DEMS. Based on the reaction pathway confirmed by in situ spectroscopy, we

calculated the Gibbs free energies of reaction intermediates on O_V–Co_3O_4 (311) and Co_3O_4 (311). As displayed in Fig. 2j, the energy barrier for NO_3^- adsorption on bare Co_3O_4 reaches up to 1.28 eV, which is recognized as the rate-determining step (RDS). The introduction of O_V results in a significantly reduced energy barrier for NO_3^- adsorption, revealing the pivotal role of O_V in the NO_3^--to-NO_2^- step. Furthermore, O_V–Co_3O_4 enables improved hydrogenation ability in the NO_2^--to-NH_3 step compared with Co_3O_4, as uncovered by the reduced energy barrier for hydrogenation of *NO to *NOH. This observation agrees with the results of the calculated energy for *H adsorption (Fig. 2g).

Anode catalyst characterization studies

The Cu doped $Ni(OH)_2$ (Cu–$Ni(OH)_2$) anode catalyst was synthesized by using a two-step approach (Fig. 3a), involving hydrothermal growth of Cu–$Ni(OH)_2$·xH_2O nanosheets on NF (Fig. S16, ESI†), followed by annealing to obtain Cu–$Ni(OH)_2$/NF. The crystal structure of the as-prepared Cu–$Ni(OH)_2$ is indexed into the β-$Ni(OH)_2$ phase (PDF#73-1520), as elucidated in XRD patterns (Fig. 3b). The molar ratio of Cu to Ni was determined to be 1:3 using inductively coupled plasma mass spectrometry (ICP-MS). Additionally, SEM and TEM images of Cu–$Ni(OH)_2$/NF indicate that Cu–$Ni(OH)_2$ exists as a nanosheet structure on the NF substrate (Fig. 3c and d), with no significant difference compared with bare $Ni(OH)_2$/NF (Fig. S17, ESI†). The
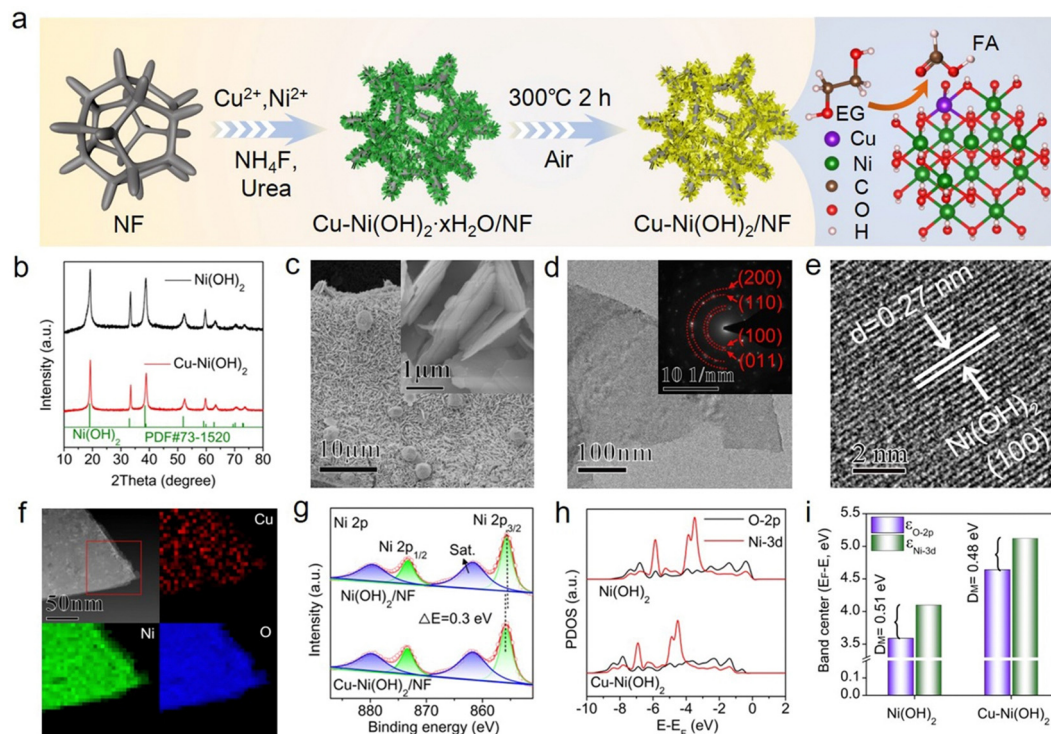
Fig. 3 Morphology and structure characterization of the anode catalyst. (a) Schematic illustration of Cu−Ni(OH)$_2$/NF preparation. (b) XRD patterns of Ni(OH)$_2$ and Cu−Ni(OH)$_2$ powders scraped from the NF substrate. (c) SEM image, (d) TEM image (the inset shows the corresponding SAED patterns), (e) HRTEM image, (f) HAADF-STEM image and its corresponding EELS maps of Cu−Ni(OH)$_2$. (g) Ni 2p XPS spectra of Ni(OH)$_2$/NF and Cu−Ni(OH)$_2$/NF. (h) PDOS of Ni(OH)$_2$ (001) and Cu−Ni(OH)$_2$/NF (001). (i) Band centers of Ni(OH)$_2$ (001) and Cu−Ni(OH)$_2$/NF (001).

lattice fringe of a spacing of 0.27 nm, observed in the HRTEM image (Fig. 3e), is attributed to the (100) plane of Ni(OH)$_2$.[44] The elemental mapping demonstrates that Cu, Ni, and O elements are uniformly dispersed on the nanosheet (Fig. 3f). The chemical states of Cu−Ni(OH)$_2$/NF were investigated *via* XPS. The Cu 2p XPS spectrum reveals that the Cu dopant is present in Cu^{2+} (Fig. S18, ESI†). In Ni 2p XPS spectra, a positive shift of 0.3 eV in the binding energy of Ni 2p can be observed for Cu−Ni(OH)$_2$/NF relative to Ni(OH)$_2$/NF (Fig. 3g), indicative of decreased charge density on the Ni site after Cu incorporation. This change in charge density results in a reduced D_M value in Cu−Ni(OH)$_2$, suggesting a greater Ni–O covalency and an enhanced ability for oxygen-containing adsorption (Fig. 3h and i).

EGOR activity and mechanism analysis

The EGOR performances of Cu−Ni(OH)$_2$/NF and Ni(OH)$_2$/NF were assessed in 1 M KOH containing 0.3 M EG at room temperature under atmospheric pressure. The reason for fixing the EG concentration at 0.3 M is elucidated in Fig. S19 (ESI†). The LSV curves show that Cu−Ni(OH)$_2$/NF requires a potential of 1.39 V to achieve a current density of 100 mA cm^{-2}, which is 60 mV lower than that of bare Ni(OH)$_2$/NF, indicating the enhanced EGOR activity due to Cu doping (Fig. 4a). Additionally, Cu−Ni(OH)$_2$/NF exhibits a higher specific EGOR activity (normalized by ECSA) than Ni(OH)$_2$/NF (Fig. S20, ESI†). Furthermore, the current density observed in LSV curves

dramatically increases for EGOR on both Ni(OH)$_2$/NF and Cu−Ni(OH)$_2$/NF compared with the OER, uncovering more thermo-dynamically favorable conditions for EGOR over the OER. To identify the impact of Cu doping concentration on EGOR activity, the Cu−Ni(OH)$_2$/NF catalysts with different Cu doping levels were synthesized (Fig. S21, ESI†). The results demon-strate that the Cu−Ni(OH)$_2$/NF catalyst with the Cu/Ni molar ratio of 1 : 3 delivers optimal EGOR activity (Fig. S22, ESI†). Unless otherwise noted, the Cu−Ni(OH)$_2$/NF catalyst in this work refers to the sample with a Cu/Ni molar ratio of 1 : 3. In addition to the high EGOR activity observed from LSV curves, Cu−Ni(OH)$_2$/NF allows faster reaction kinetics and reduced charge transfer resistance with respect to bare Ni(OH)$_2$/NF, as evidenced by the Tafel slopes (Fig. 4b) and EIS spectra (Fig. S23, ESI†).

The EGOR products during 2-h potentiostatic tests on Cu−Ni(OH)$_2$/NF and Ni(OH)$_2$/NF were identified using HPLC (Fig. S24, ESI†). Compared with Ni(OH)$_2$/NF, Cu−Ni(OH)$_2$/NF exhibits a higher FE of FA (FE$_{FA}$) across a wide potential range of 1.4 to 1.6 V (Fig. 4c). When the potential is fixed at 1.5 V, Cu−Ni(OH)$_2$/NF achieves a maximum FE$_{FA}$ of 98%, along with a FA productivity of 5.92 mmol cm^{-2} h^{-1}, surpassing the perfor-mance of most recently reported EGOR catalysts (Table S2, ESI†). Intriguingly, when a total electric charge of 2000 C is transferred through the entire cell, Cu−Ni(OH)$_2$/NF achieves an EG conversion of 97% and a FA yield of 89%, with the production of a small amount of glycolic acid (GA) byproduct
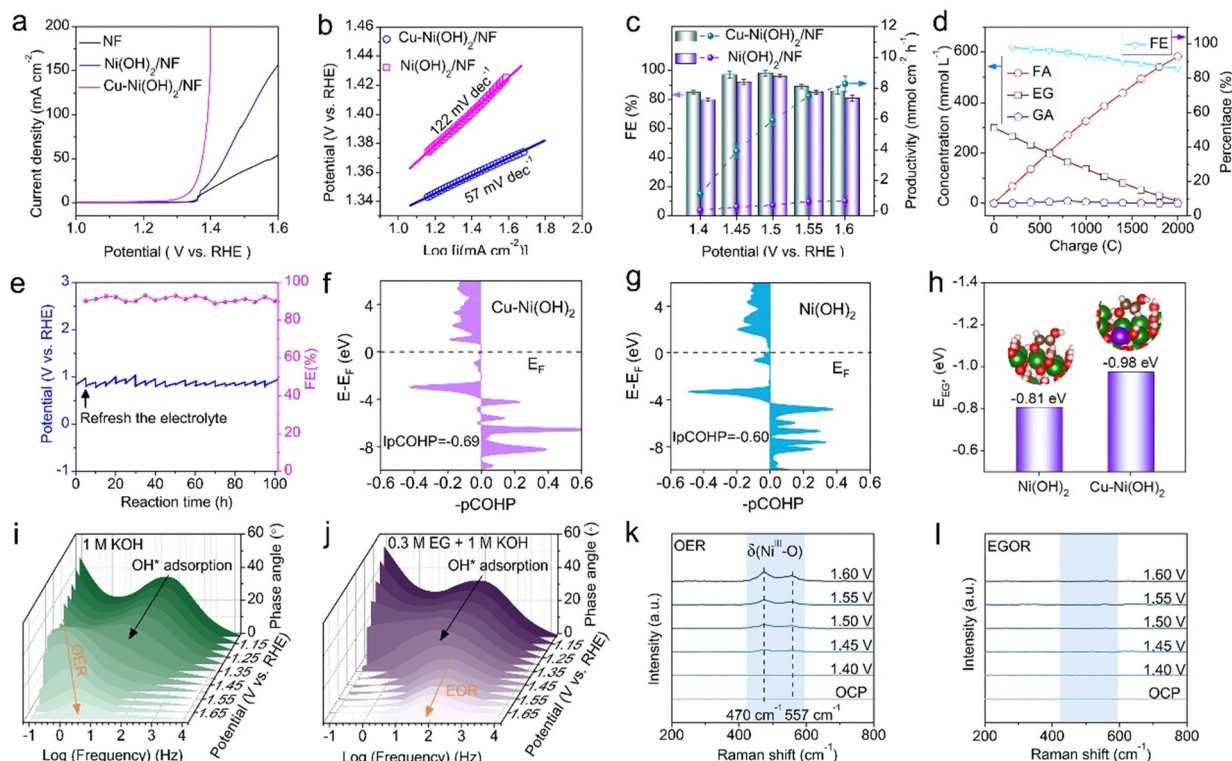
Fig. 4 EGOR activity and enhanced mechanism. (a) Polarization curves of Ni(OH)$_2$/NF and Cu−Ni(OH)$_2$/NF measured in 1 M KOH with and without 0.3 M EG. (b) Tafel slopes of Ni(OH)$_2$/NF and Cu−Ni(OH)$_2$/NF. (c) The FE and productivity of FA on Ni(OH)$_2$/NF and Cu−Ni(OH)$_2$/NF under various potentials. (d) Concentrations of FA, GA, EG, and FE of FA as a function of consumed charges. (e) Stability tests using chronopotentiometry measurements at the current density of 100 mA cm^{-2}, and the electrolyte was refreshed every 5 h. (f) and (g) The computed pCOHP diagrams of Ni−O$_{ads}$ bond on Cu−Ni(OH)$_2$ (f) and Ni(OH)$_2$ (g). (h) The calculated energy for EG adsorption on Cu−Ni(OH)$_2$ (001) and Ni(OH)$_2$ (001). (i) and (j) Bode phase plots of the operando EIS on Cu−Ni(OH)$_2$/NF in 1 M KOH (i) and 1 M KOH + 0.3 EG (j). (k) and (l) *In situ* Raman tests on Cu−Ni(OH)$_2$ under varying potentials in 1 M KOH (k) and 1 M KOH + 0.3 EG (l).

(Fig. 4d and Fig. S25, ESI†), indicating the highly selective conversion of EG to FA. The long-term stability of Cu–Ni(OH)$_2$/NF for EGOR was performed at a current density of 100 mA cm^{-2} (Fig. 4e). Impressively, the FE$_{FA}$ value is consistently maintained at around 90% throughout the 100-h operation period. The recovered Cu–Ni(OH)$_2$/NF catalyst was characterized by using various techniques, including SEM, TEM, XRD, and XPS (Fig. S26–S28, ESI†). These results show that the used catalyst retains the original morphology and structure, indicating the stability of Cu–Ni(OH)$_2$/NF.

To understand the underlying mechanism responsible for the enhanced EGOR performance on Cu–Ni(OH)$_2$/NF, the projected crystal orbital Hamilton populations (pCOHP) were performed (Fig. S29, ESI†), which is used to elucidate the Ni–O$_{ads}$ bonding state (O$_{ads}$ is from the adsorbed EG species).[45] It is well-accepted that a negative value of integrated pCOHP (IpCOHP) indicates a stable Ni–O$_{ads}$ bonding state.[41] As depicted in Fig. 4f and g, the IpCOHP value relative to the Fermi level is calculated to be −0.69 for Ni–O$_{ads}$ on the Cu–Ni(OH)$_2$ (001) surface, lower than that (−0.60) for Ni–O$_{ads}$ on the Ni(OH)$_2$ (001) surface, suggesting an enhanced bonding interaction between Ni and EG upon Cu doping. Furthermore, the EG adsorption energy calculations confirm a more thermodynamically favorable EG adsorption on Cu–Ni(OH)$_2$ (Fig. 4h).

To experimentally verify the enhanced EG adsorption on Cu–Ni(OH)$_2$, open-circuit potential (OCP) measurements were performed. As shown in Fig. S30 (ESI†), the OCP change over Cu–Ni(OH)$_2$ is determined to be 0.32 V, significantly higher than bare Ni(OH)$_2$ (0.06 V), indicating the favorable EG adsorption on Cu–Ni(OH)$_2$.[46] The interfacial behaviors were investigated using Operando EIS at various potentials. When the EG feedstock is added, the Nyquist semicircle in the low-frequency region at 1.4 V becomes apparent (Fig. 4i and j), indicating the appearance of EGOR.[47] This observation agrees with the oxidation potential observed from the LSV curves (Fig. 4a). Upon further increasing the potentials, the EGOR peak gradually shifts to lower phase degrees. These results suggest that EGOR is thermodynamically more favorable than OER in the presence of EG.[48] The EGOR mechanism over Cu–Ni(OH)$_2$ was investigated using *in situ* Raman measurements. Under OER conditions, a pair of characteristic bands at 470 and 557 cm^{-1}, corresponding to NiOOH,[49] are observed at 1.4 V (Fig. 4k). The band intensities of NiOOH increase with increasing potential, indicating surface reconstruction on Cu–Ni(OH)$_2$. Upon EG addition, the NiOOH signals completely disappeared and the catalyst reverts to its initial Cu–Ni(OH)$_2$ (Fig. 4l), indicating that EGOR proceeds *via* an indirect oxidation way on Cu–Ni(OH)$_2$.[50]

Co-production of NH₃ and FA

Encouraged by the high activities for half-reaction NO_3^-RR and EGOR, we attempted to integrate the NO_3^-RR and EGOR in a two-electrode membrane–electrode assembly (MEA) system separated by a proton exchange membrane (PEM) (Fig. 5a). The as-prepared Cu–Ni(OH)₂/NF and O_V–Co₃O₄/NF served as the anode and cathode, respectively. The LSV curves show that, to obtain a current density of 100 mA cm⁻², the paired NO_3^-RR//EGOR system only requires a cell voltage of 1.66 V, markedly lower than that (2.20 V) for the conventional NO_3^-RR//OER system (Fig. 5b). This disparity suggests that the replacement of the OER by EGOR contributes to reducing the overall energy input. To assess the coupled performance in the two-electrode system, the FEs of FA and NH₃ were measured under different current densities during 2-h electrolysis. It can be observed that Cu–Ni(OH)₂/NF enables stable and high FE for

FA production (>95%) across a wide current density range from 25 to 100 mA cm⁻². In contrast, NO_3^-RR activity exhibits a volcano-type trend, with a current density of 100 mA cm⁻² being recognized as optimal for NH₃ production. At higher current densities (>100 mA cm⁻²), the observed reduction in the FE of NH₃ is attributed to the competitive hydrogen evolution reaction.

The practical application of this paired system was subsequently carried out using real-world PET bottles and simulated nitrate wastewater as the initial feedstock (Fig. 5d and Fig. S31, ESI†). Prior to co-electrolysis, 100 g of post-consumer plastic bottles were collected and hydrolyzed into their constituent monomers using KOH (Fig. S32, ESI†). The resulting hydrolysate was directly fed into the anodic chamber. As for the cathodic feedstock, a simulated high-concentration nitrate solution was prepared via electrodialysis, following established
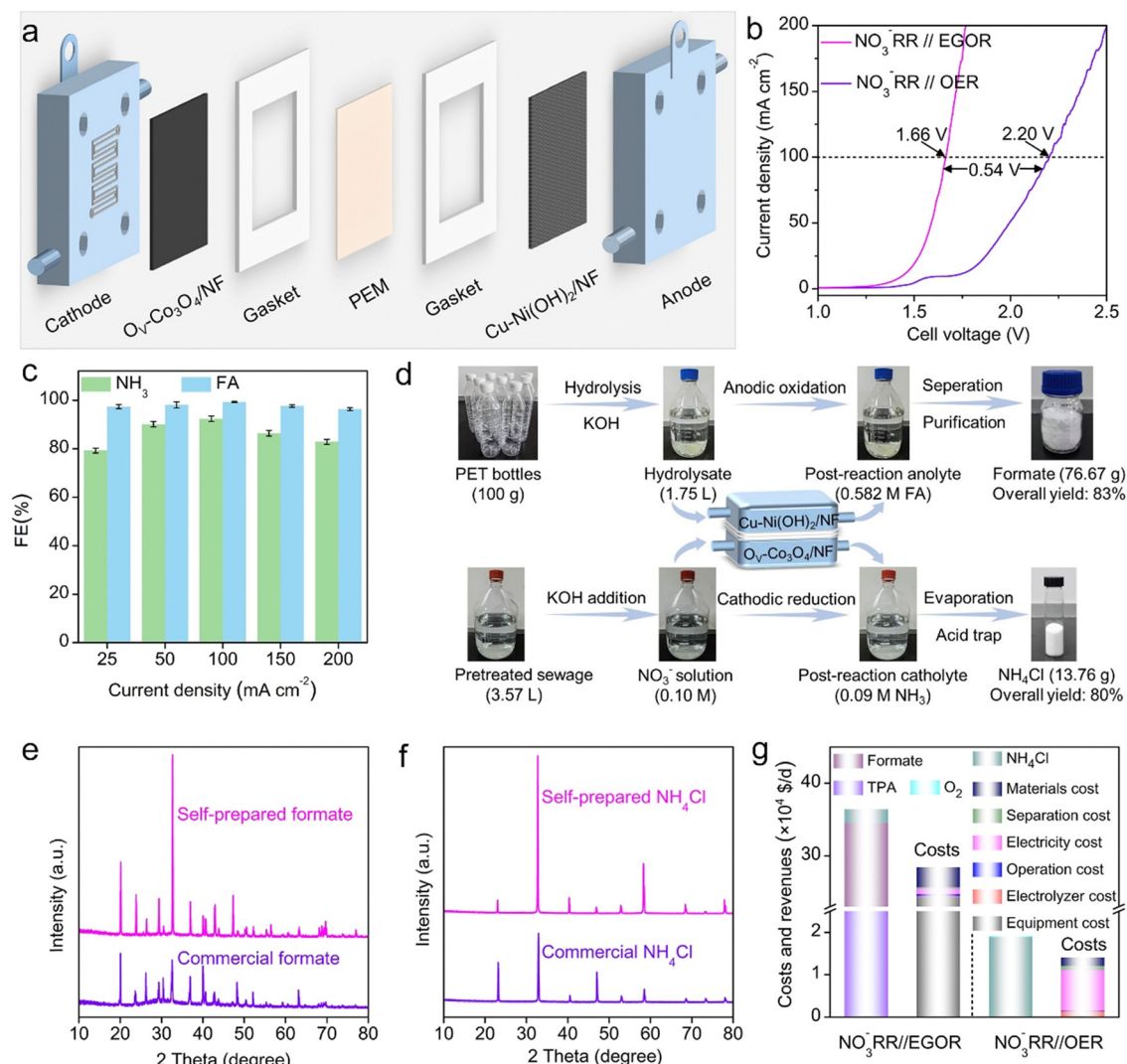
Fig. 5 Integration of the NO_3^-RR and EGOR. (a) Schematic diagram showing the two-electrode MEA reactor for NO_3^-RR coupled with EGOR. (b) Comparison of the LSV curves for NO_3^-RR//OER and NO_3^-RR//EGOR system. (c) The FEs of NH₃ and FA measured under different current densities. (d) Schematic illustration of formate and NH₄Cl production from PET bottle and nitrate wastewater. (e) and (f) XRD patterns of synthesized formate (e) and NH₄Cl (f). (g) TEA of NO_3^-RR//OER and NO_3^-RR//EGOR system.

protocols from previous literature.[15] Of note, KOH was added as electrolyte prior to electrochemical valorization. After 210-h electrolysis (Fig. S33, ESI†), FA was identified as the primary product in the anolyte, evidenced by ^{1}H nuclear magnetic resonance (NMR) (Fig. S34, ESI†). Following separation and purification, 76.67 g of formate were obtained (FA exists as formate under alkaline conditions), with an overall yield of 83%. In parallel, NH_3 was generated at the cathode with an 80% yield, resulting in 13.76 g of NH_4Cl crystals after acidification and evaporation. The high purity of formate and NH_4Cl was confirmed via XRD patterns, FTIR spectra, and ^{1}H NMR (Fig. 5e and f and Fig. S35 and S36, ESI†). To assess the economic viability of our constructed NO_3^-RR//EGOR system, a TEA was conducted (Fig. 5g and Note S1, ESI†). The TEA results indicate that our coupled system achieves a higher gross profit (79665.9 \$ d^{-1}), corresponding to a 15-fold increase than the conventional NO_3^-RR// OER system (5173.4 \$ d^{-1}), which indicates the potential market competitiveness of our built electrosynthesis system.

Conclusions

In this work, we constructed a paired electrolysis system with low energy input comprising cathodic reduction of NO_3^- to NH_3 and anodic oxidation of PET-derived EG to FA, which is made possible by the discovery of the O_V–Co_3O_4 cathode and Cu–$Ni(OH)_2$ anode. The O_V incorporation compensates for the deficiencies of bare Co_3O_4 in terms of NO_3^- adsorption and activation. Cu doping enlarges the Ni–O covalency, thus resulting in an enhanced capability for EG adsorption. Under optimal conditions, this paired electrochemical system achieves 13.76 g of high-purity NH_4Cl crystals with an 80% yield from simulated waster and 76.67 g of formate with an 83% yield from postconsumer PET bottles. Overall, this work provides a cost-effective and low-carbon route to mitigate wastes while producing valuable chemicals.

Author contributions

B. Qiu and Y. Zhang supervised the project and conceived the idea. B. Qiu, N. Zhang, M. Du, and M. Han designed all experiments and co-wrote the manuscript. M. Du, T. Sun, and X. Guo performed the materials synthesis and characterization studies. M. Du, W. Chen, M. Han, and J. Ma carried out electrocatalytic measurements. J. Shang performed the DFT simulations. V. Nicolosi and C. Zhou provided suggestions for the characterization studies. All authors provided comments on the manuscript.

Data availability

The data supporting this article have been included as part of the ESI.†

Conflicts of interest

There are no conflicts to declare.

Acknowledgements

References

1 G.-F. Han, F. Li, Z.-W. Chen, C. Coppex, S.-J. Kim, H.-J. Noh, Z. Fu, Y. Lu, C. V. Singh, S. Siahrostami, Q. Jiang and J.-B. Baek, *Nat. Nanotechnol.*, 2021, **16**, 325–330.

2 S. Li, Y. Zhou, X. Fu, J. B. Pedersen, M. Saccoccio, S. Z. Andersen, K. Enemark-Rasmussen, P. J. Kempen, C. D. Damsgaard, A. Xu, R. Sažinas, J. B. V. Mygind, N. H. Deissler, J. Kibsgaard, P. C. K. Vesborg, J. K. Nørskov and I. Chorkendorff, *Nature*, 2024, **629**, 92–97.

3 S. Li, X. Fu, J. K. Nørskov and I. Chorkendorff, *Nat. Energy*, 2024, **9**, 1344–1349.

4 M. Wang, M. A. Khan, I. Mohsin, J. Wicks, A. H. Ip, K. Z. Sumon, C.-T. Dinh, E. H. Sargent, I. D. Gates and M. G. Kibria, *Energy Environ. Sci.*, 2021, **14**, 2535–2548.

5 D. Ye and S. C. E. Tsang, *Nat. Synth.*, 2023, **2**, 612–623.

6 K. Chu, Y. Luo, P. Shen, X. Li, Q. Li and Y. Guo, *Adv. Energy Mater.*, 2022, **12**, 2103022.

7 S. Han, H. Li, T. Li, F. Chen, R. Yang, Y. Yu and B. Zhang, *Nat. Catal.*, 2023, **6**, 402–414.

8 J. Hao, T. Wang, R. Yu, J. Cai, G. Gao, Z. Zhuang, Q. Kang, S. Lu, Z. Liu and J. Wu, *Nat. Commun.*, 2024, **15**, 9020.

9 K. Kim, A. Zagalskaya, J. L. Ng, J. Hong, V. Alexandrov, T. A. Pham and X. Su, *Nat. Commun.*, 2023, **14**, 823.

10 M. Du and B. Qiu, *Nat. Water*, 2024, **2**, 1053–1054.

11 P. H. van Langevelde, I. Katsounaros and M. T. Koper, *Joule*, 2021, **5**, 290–294.

12 M. Duca and M. T. Koper, *Energy Environ. Sci.*, 2012, **5**, 9726–9742.

13 G. Qing, R. Ghazfar, S. T. Jackowski, F. Habibzadeh, M. M. Ashtiani, C.-P. Chen, M. R. Smith, III and T. W. Hamann, *Chem. Rev.*, 2020, **120**, 5437–5516.

14 M. Li, X. Liu, L. Wang, F. Hou, S. X. Dou and J. Liang, *EcoMat*, 2021, **3**, e12096.

15 F.-Y. Chen, A. Elgazzar, S. Pecaut, C. Qiu, Y. Feng, S. Ashokkumar, Z. Yu, C. Sellers, S. Hao, P. Zhu and H. Wang, *Nat. Catal.*, 2024, **7**, 1032–1043.

16 Y. Liu, Z. Zhuang, Y. Liu, N. Liu, Y. Li, Y. Cheng, J. Yu, R. Yu, D. Wang and H. Li, *Angew. Chem., Int. Ed.*, 2024, **63**, e202411396.

17 C. Li, H. Li, B. Zhang, H. Li, Y. Wang, X. Wang, P. Das, Y. Li, X. Wu, Y. Li, Y. Cui, J. Xiao and Z.-S. Wu, *Angew. Chem., Int. Ed.*, 2024, **63**, e202411542.

18 Q. Hu, S. Qi, Q. Huo, Y. Zhao, J. Sun, X. Chen, M. Lv, W. Zhou, C. Feng, X. Chai, H. Yang and C. He, *J. Am. Chem. Soc.*, 2024, **146**, 2967–2976.

19 S. Qi, Z. Lei, Q. Huo, J. Zhao, T. Huang, N. Meng, J. Liao, J. Yi, C. Shang, X. Zhang, H. Yang, Q. Hu and C. He, *Adv. Mater.*, 2024, **36**, 2403958.

20 J. Yan, P. Liu, J. Li, H. Huang and W. Song, *Small*, 2024, **20**, 2308617.

21 Z. Fan, C. Cao, X. Yang, W. Yuan, F. Qin, Y. Hu, X. Sun, G. Liu, Y. Tian and L. Xu, *Angew. Chem., Int. Ed.*, 2024, **63**, e202410356.

22 J.-Y. Fang, Q.-Z. Zheng, Y.-Y. Lou, K.-M. Zhao, S.-N. Hu, G. Li, O. Akdim, X.-Y. Huang and S.-G. Sun, *Nat. Commun.*, 2022, **13**, 7899.

23 K. Zhang, P. Sun, Y. Huang, M. Tang, X. Zou, Z. Pan, X. Huo, J. Wu, C. Lin, Z. Sun, Y. Wan, X. Zhang and L. An, *Adv. Funct. Mater.*, 2024, **34**, 2405179.

24 M. Zhang, Z. Ma, S. Zhou, C. Han, V. Kundi, P. V. Kumar, L. Thomsen, B. Johannessen, L. Peng, Y. Shan, C. Tsounis, Y. Yang, J. Pan and R. Amal, *ACS Catal.*, 2024, **14**, 11231–11242.

25 S. Kang, X. Guo, D. Xing, W. Yuan, J. Shang, V. Nicolosi, N. Zhang and B. Qiu, *Small*, 2024, **20**, 2406068.

26 K. Chu, W. Zong, G. Xue, H. Guo, J. Qin, H. Zhu, N. Zhang, Z. Tian, H. Dong, Y.-E. Miao, M. B. J. Roeffaers, J. Hofkens, F. Lai and T. Liu, *J. Am. Chem. Soc.*, 2023, **145**, 21387–21396.

27 Y. Li, J. Ma, Z. Wu and Z. Wang, *Environ. Sci. Technol.*, 2022, **56**, 8673–8681.

28 J. Li, H. Li, K. Fan, J. Y. Lee, W. Xie and M. Shao, *Chem Catal.*, 2023, **3**, 100638.

29 Y. Yang, J. Liu, M. Ahmad, X.-Q. Sun, C. Liu, S. Chen, J. Zhang, J.-L. Luo and X.-Z. Fu, *Chem. Eng. J.*, 2025, **505**, 159653.

30 S.-Q. Liu, S. Xie, S. Wu, Y. Yang, P.-X. Lei, S. Luo, R. Feng, X.-Z. Fu and J.-L. Luo, *Adv. Funct. Mater.*, 2024, **34**, 2404105.

31 M. Du, R. Xue, W. Yuan, Y. Cheng, Z. Cui, W. Dong and B. Qiu, *Nano Lett.*, 2024, **24**, 9768–9775.

32 T. Ren, Z. Duan, H. Wang, H. Yu, K. Deng, Z. Wang, H. Wang, L. Wang and Y. Xu, *ACS Catal.*, 2023, **13**, 10394–10404.

33 M. Du, M. Xing, S. Kang, Y. Ma, B. Qiu and Y. Chai, *EcoMat*, 2022, **4**, e12259.

34 Y. Ma, X. Guo, M. Du, S. Kang, W. Dong, V. Nicolosi, Z. Cui, Y. Zhang and B. Qiu, *Green Chem.*, 2024, **26**, 3995–4004.

35 Y. Ma, Y. Zhang, M. Xing, S. Kang, M. Du, B. Qiu and Y. Chai, *Chem. Commun.*, 2022, **58**, 6642–6645.

36 Z. Xiao, Y.-C. Huang, C.-L. Dong, C. Xie, Z. Liu, S. Du, W. Chen, D. Yan, L. Tao and Z. Shu, *J. Am. Chem. Soc.*, 2020, **142**, 12087–12095.

37 H. Idriss, *Surf. Sci.*, 2021, **712**, 121894.

38 T. J. Frankcombe and Y. Liu, *Chem. Mater.*, 2023, **35**, 5468–5474.

39 Y. Ma, H. Tao, X. Guo, P. Yang, D. Xing, V. Nicolosi, Y. Zhang, C. Lian and B. Qiu, *J. Mater. Chem. A*, 2024, **12**, 27220–27228.

40 Y. Sun, H. Liao, J. Wang, B. Chen, S. Sun, S. J. H. Ong, S. Xi, C. Diao, Y. Du and J.-O. Wang, *Nat. Catal.*, 2020, **3**, 554–563.

41 N. Zhang, J. Shang, X. Deng, L. Cai, R. Long, Y. Xiong and Y. Chai, *ACS Nano*, 2022, **16**, 4795–4804.

42 C. Zhou, Y. Zhang, C. Xie, J. Bai, J. Li, H. Zhang, H. Zhu, M. Long, B. Zhou and G. Zheng, *Environ. Sci. Technol.*, 2024, **58**, 14940–14948.

43 J. Ni, J. Yan, F. Li, H. Qi, Q. Xu, C. Su, L. Sun, H. Sun, J. Ding and B. Liu, *Adv. Energy Mater.*, 2024, **14**, 2400065.

44 F. Ma, Y. Wen, P. Fu, J. Zhang, Q. Tang, T. Chen, W. Luo, Y. Zhou and J. Wang, *Small*, 2024, **20**, 2305767.

45 Y.-C. Hao, Y. Guo, L.-W. Chen, M. Shu, X.-Y. Wang, T.-A. Bu, W.-Y. Gao, N. Zhang, X. Su and X. Feng, *Nat. Catal.*, 2019, **2**, 448–456.

46 M. Du, Y. Zhang, S. Kang, C. Xu, Y. Ma, L. Cai, Y. Zhu, Y. Chai and B. Qiu, *Small*, 2023, **19**, 2303693.

47 M. Song, Y. Wu, Z. Zhao, M. Zheng, C. Wang and J. Lu, *Adv. Mater.*, 2024, **36**, 2403234.

48 F. Ma, Z. Li, R. Hu, Z. Wang, J. Wang, J. Li, Y. Nie, Z. Zheng and X. Jiang, *ACS Catal.*, 2023, **13**, 14163–14172.

49 H. Zhong, Q. Zhang, J. Yu, X. Zhang, C. Wu, Y. Ma, H. An, H. Wang, J. Zhang and X. Wang, *Adv. Energy Mater.*, 2023, **13**, 2301391.

50 W. Luo, H. Tian, Q. Li, G. Meng, Z. Chang, C. Chen, R. Shen, X. Yu, L. Zhu and F. Kong, *Adv. Funct. Mater.*, 2024, **34**, 2306995.